# Lab Notes

**Editors**
Thomas M. Moses | Shane F. McClure

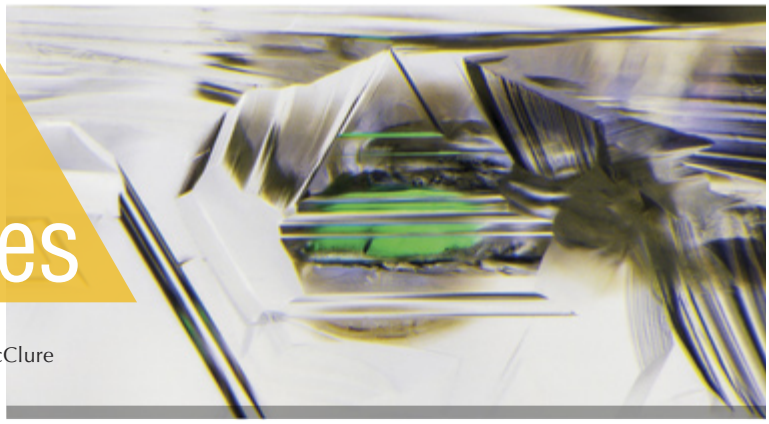

## Atypical Dyed BERYL

A green stone mounted in a ring was recently submitted to the New York lab. The ring's prongs prevented a full reading of the stone's refractive index, but a maximum reading of 1.578 indicated the material was potentially beryl. Face-up, the even distribution of color made an identification of emerald appear likely (figure 1). However, careful microscopic examination revealed an even distribution of thin green zoning resembling mica platelets typical of amazonite (figure 2). Oblique fiber-optic lighting exposed a network of incipient basal cleavage perpendicular to the c-axis (figure 3). Using a handheld spectroscope, a characteristic of dyed green beryl was observed: a broad absorption band in the red region in the absence of chromium lines. Denser green color concentrations were also present in larger surface-reaching fissures.

While dyed beryl is occasionally submitted to GIA, it is mostly translucent and immediately identifiable due to its unnatural color. This impressive emerald imitation was the first of its kind submitted to the New York or Carlsbad labs. It serves as an important reminder that careful, methodical gemological testing is necessary to detect these subtler treatments.

*Tyler Smith*

*Figure 1. A mounted green stone with a superficial resemblance to emerald was later revealed to be dyed beryl.*

## CVD Laboratory-Grown DIAMOND With Counterfeit GIA Inscription

In recent months, GIA has seen a number of laboratory-grown diamonds submitted for update or verification services with counterfeit inscriptions referencing GIA natural diamond reports ("GIA laboratory prevents attempted fraud," GIA press release, May 17, 2021, https://www.gia.edu/gia-news-press/gia-lab-prevents-attempted-fraud). One recent example is a 3.07 ct round brilliant submitted to the Antwerp lab for update service (figure 4). It bore an inscription matching a GIA report for a natural diamond that had been submitted in 2018. Microscopic examination quickly revealed,

*Figure 2. Thin, evenly distributed concentrations of green dye in the beryl, as seen through the table. Field of view 1.76 mm.*

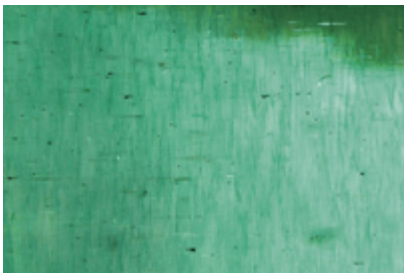

*Figure 3. Basal cleavage under oblique illumination. Shallow cavities can be seen toward the top, where the fissures reach the surface of the stone. Field of view 2.90 mm.*

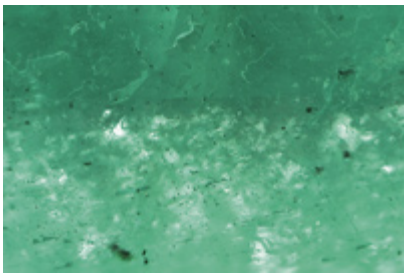

*Editors' note: All items were written by staff members of GIA laboratories.*

Gems & Gemology, Vol. 57, No. 2, pp. 150–157.

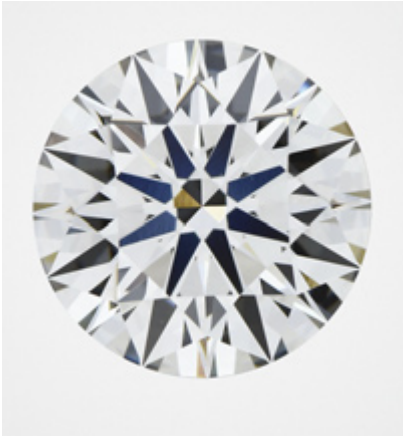

*Figure 4. This 3.07 ct CVD lab-grown diamond was submitted with a counterfeit GIA inscription that corresponded to a previously graded natural diamond.*

**TABLE 1.** Comparison of the natural diamond submitted to GIA in 2018 and the laboratory-grown diamond submitted with a counterfeit inscription in 2021.

| | Natural | Laboratory-grown |
|---|---|---|
| Weight (ct) | 3.078 | 3.075 |
| Shape | Round brilliant | Round brilliant |
| Measurements (mm) | 9.33–9.38 x 5.74 | 9.39–9.41 x 5.76 |
| Girdle | Slightly thick | Medium |
| Cut | Excellent | Excellent |
| Symmetry | Excellent | Excellent |
| Polish | Excellent | Excellent |
| Color | G | H |
| Long-wave UV fluorescence | None | None |
| Clarity | IF | $VVS_2$ |
| Inclusions | - | Pinpoints, needles |
| Diamond type | Ia | IIa |

however, that the inscription was in fact fraudulent. Further analysis indicated a laboratory-grown origin.

Comparison showed an attempt to precisely match the laboratory-grown diamond to the information contained in the original report (table 1). Both were round brilliants with excellent cut properties and very close in carat weight and measurements. The natural diamond, however, did have a slightly better color and clarity (G-IF compared to H-$VVS_2$). The clarity grade of the laboratory-grown diamond ($VVS_2$) was set by two types of inclusions: pinpoints and needles.

Further analysis of the laboratory-grown diamond was performed using advanced spectroscopic techniques. Whereas the original diamond was type Ia and had a high concentration of nitrogen such that it saturated the detector in the one- phonon region (1335–1085 $cm^{-1}$), Fourier-transform infrared (FTIR) analysis revealed that the newly submitted diamond was nominally type IIa. The spectrum showed the weak presence of isolated nitrogen at 1344 $cm^{-1}$ and the absence of both the 3107 $cm^{-1}$ and the CVD-specific $NVH^0$ band at 3123 $cm^{-1}$. Photoluminescence (PL) spectra taken with various laser excitation wavelengths and at liquid nitrogen temperature showed the strong presence of the $SiV^-$ doublet (736.6/736.9 nm), a defect commonly observed in CVD laboratory-grown diamonds. This strong $SiV^-$ center was also conspicuous in the UV-Visible absorption spectrum taken at liquid nitrogen temperature. Other defects detected with PL spectroscopy were strong $NV^{0/-}$ (575 and 637 nm) centers, a strong H3 (503.2 nm) center, and weak nickel-related defects (883/884 nm doublet).

DiamondView imaging displayed a typical CVD growth structure with a green-blue layered pattern and banded layers, indicating a start-stop growth (figure 5). A weak greenish blue phosphorescence was observed after switching off the UV source.

Based on all the observations, we concluded this was a CVD laboratory-grown diamond that had undergone HPHT treatment after growth. As with all laboratory-grown diamonds submitted to GIA, it was then inscribed with "LABORATORY-GROWN" (figure 6, left). The

*Figure 5. DiamondView imaging confirmed CVD growth and subsequent HPHT treatment.*

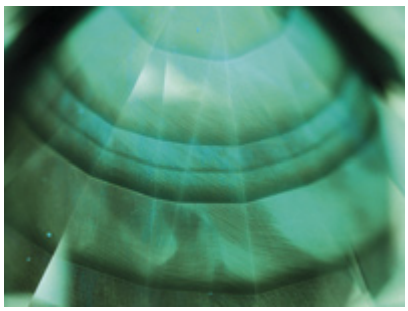

*Figure 6. In accordance with GIA procedures, the LABORATORY-GROWN inscription was added to the girdle (left) and the counterfeit report number inscription was rendered illegible (right).*

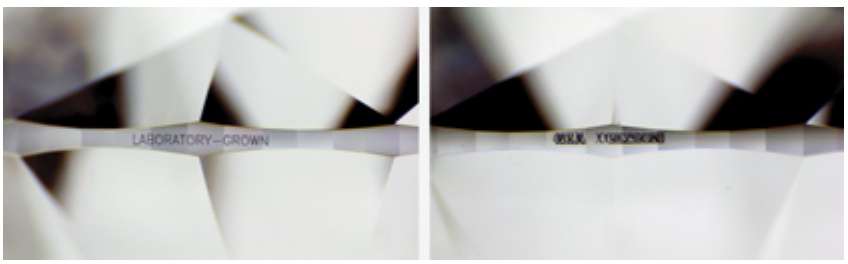

*Figure 7. A Melo pearl measuring 20.50 × 19.25 × 18.85 mm and weighing 55.10 ct. A fine crack is visible across the center of the surface.*

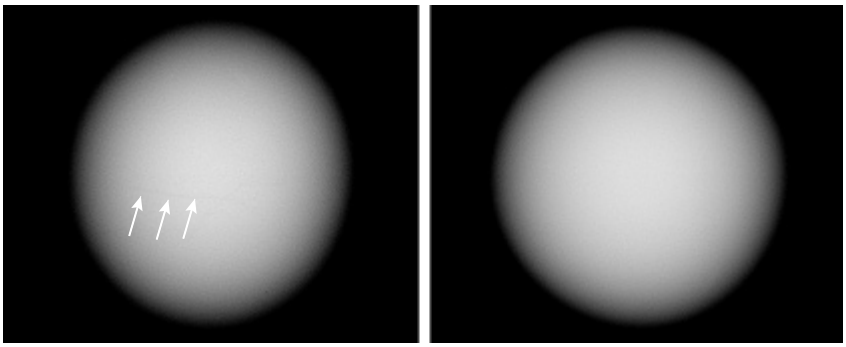

*Figure 9. Microradiographs in two directions showed no obvious internal growth structure. Only a fine dark line showed in one orientation, which corresponded to a surface-reaching crack (left, indicated by the white arrows).*

counterfeit inscription was overwritten (figure 6, right) and a new GIA report number was placed on the girdle.

This example demonstrates the importance of careful examination to verify a diamond's origin. A close comparison of the CVD diamond with the earlier report on a natural diamond showed a very precise attempt at matching.

*Ellen Barrie and Sally Eaton-Magaña*

## Melo PEARL Found in a Melo Shell

Over the years, there have been a number of reports relating discoveries of natural pearls in edible oysters (e.g., Fall 2019 Gem News International, pp. 439–440; Fall 2020 Lab Notes, pp. 420–422). However, similar discoveries are much rarer in gastropods, such as species of the *Melo* genus. Such finds often make headlines, as was the case recently in Thailand when a few discoveries were reported on social media. One of these remarkable stories, titled "A delicious find," was posted on www.facebook.com/GIAEducation on April 9, 2021. It detailed the discovery of a large oval orange Melo pearl measuring 20.50 × 19.25 × 18.85 mm and weighing 55.10 ct that was submitted to GIA's Bangkok laboratory for testing in September 2020 (figure 7). The owner claimed to have accidentally found this pearl in an inexpensive Melo shell he purchased with another shell from a local market in Rayong Province, eastern Thailand.

This note offers additional detail on the pearl that was the subject of that story. To the eye, the pearl looked exactly as a Melo pearl should. Its size and color were consistent with that type of pearl, and it exhibited various flame structure patterns on its surface: short patchy flames, thin elongated flames, and "triangular" flames reminiscent of Christmas trees (figure 8). These features were consistent with flame structures previously observed on Melo pearls (D.J. Content, Ed., *Pearl and the Dragon: A Study of Vietnamese Pearls and a History of the Oriental Pearl Trade*, Houlton, Maine, 1999, pp. 90–92; H. Htun et al., "Melo 'pearls' from Myanmar," Fall 2006 *G&G*, pp. 135–136; V. Pardieu, "Concise Field Report: Melos and their pearls in Vietnam," *GIA Research News*, https://www.gia.edu/ongoing-research/melo-pearls-from-vietnam, 2009). Some other associated minor surface features were visible, together with a long fine crack traversing one area (figure 8, left). Microradiography revealed no obvious internal growth structure (figure 9). Only the fine crack previously mentioned showed

*Figure 8. Various flame structure patterns visible on the pearl's surface: short patchy flames with a fine surface-reaching crack (left), thin elongated flames with some minor natural features (center), and flames reminiscent of Christmas trees (right). Fields of view 19.20, 7.20, and 3.60 mm, respectively.*

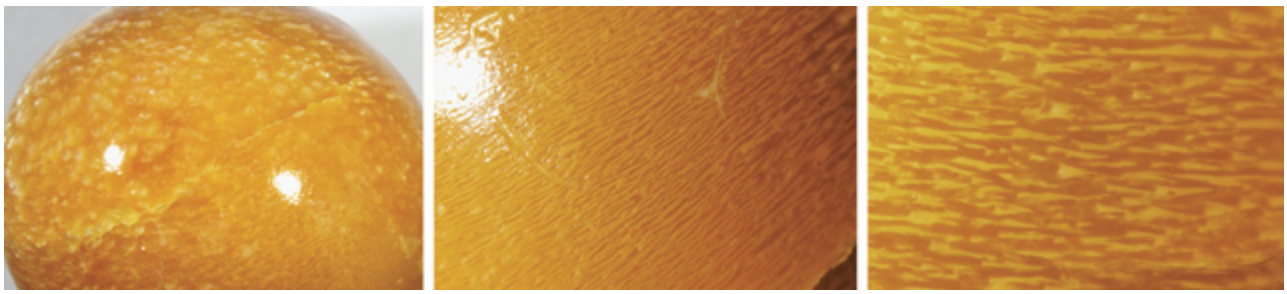

as a dark fine line in the correct orientation (figure 9, left, indicated by the white arrows). The absence of any surface modification and the presence of natural surface features, in addition to the lack of banded structure typically observed in shell samples, proved this was a pearl and not an imitation fashioned from Melo shell (Summer 2006 Lab Notes, pp 166–167; N. Sturman et al., "An imitation Melo pearl," *GIA Research News*, https://www.gia.edu/gia-news-research/imitation-melo-pearl, 2011).

Spectral analyses using Raman, photoluminescence (PL), and UV-Visible (UV-Vis) spectroscopy proved the pearl's color was of natural origin. Raman spectra revealed features at 701, 705, and 1085 $cm^{-1}$ identifying aragonite, together with polyenic peaks at 1130 and 1520 $cm^{-1}$ responsible for the orange coloration. These polyenic peaks are consistent with other naturally colored porcelaneous pearls (S. Karampelas et al., "Polyacetylenic pigments found in pearls and corals," *30th International Gemmological Conference Proceedings*, 2007, pp. 49–51; Summer 2018 Lab Notes, pp. 211–212).

An interesting declaration made by the pearl's owner probably explains the presence of the fine eye-visible surface crack. The Melo shell containing the hidden pearl was boiled, and the Melo pearl was only discovered when the meat was being prepared for consumption. Hence, it is likely that the temperatures and duration applied during the cooking process caused the crack's formation. This point has been mentioned by a number of pearl traders during discussions with lab gemologists over the years, so it seems an important consideration when such cracks are observed. Even so, the notable size, unmodified surface, perfectly formed oval shape, and intense natural color all combined to make this a desirable and special pearl.

*Nanthaporn Nilpetploy*

## Imitation MOLDAVITE

Recently GIA's Carlsbad laboratory received for identification a 46.13 ct yellowish green rough stone. The lack of a polished flat surface prevented a refractive index reading, while the specific gravity was measured as 2.45. Under microscopic examination, very few gas bubbles were found and some straight, approximately evenly spaced surface features were observed (figure 10). Closer examination revealed these features were likely artificially acid-etched flow lines. The presence of gas bubbles coupled with flow lines led the author to infer an artificial glass or a natural glass, possibly moldavite, though moldavite has more natural-looking flow lines (figure 11). The SG reading was also slightly higher than the expected SG of 2.36 for moldavite. Additionally, moldavite typically contains numerous gas bubbles. Suspecting an artificial glass, the author analyzed the stone with a Fourier-transform infrared (FTIR) spectrometer. The FTIR reading showed absorption bands at approximately 2900 and 3480 nm, which confirmed an artificial glass.

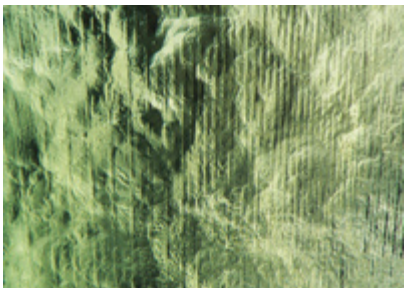

*Figure 10. Acid-etched flow lines on artificial glass imitating moldavite. Field of view 2.34 mm.*

Moldavites are a form of tektite, an impact glass created by the melting of rock caused when a meteorite strikes the earth's surface. The most famous moldavites, found in southern Bohemia in the Czech Republic, were formed by the impact of the meteor that created the Ries crater 500 km away in southern Germany 14.7 million years ago. With rising prices for moldavite over the past few years, moldavite imitations have become more prevalent (Spring 2015 Gem News International, pp. 103–104).

*Figure 11. Natural flow lines on moldavite. Field of view 7.19 mm.*

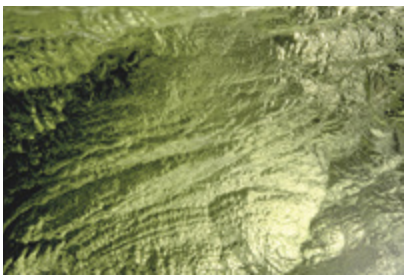

*Michaela Stephan*

## Exquisite OPAL Strand

The Carlsbad laboratory recently received for identification a strand of 28 graduated round gray beads displaying spectacular play-of-color (figure 12). At the time of inspection, the strand weighed 115.5 grams total. Standard gemological properties were consistent with opal. All 28 beads had a spot RI reading of approximately 1.39 and fluoresced very weak yellow under short-wave UV and weak yellow to long-wave UV. No indications of dye, color treatment, clarity enhancement, or coating were present. All of the beads showed a natural play-of-color phenomenon under microscopic examination. A single drop of water was placed on the surface of each bead and observed under direct transmitted light in brightfield mode in the microscope. Each bead absorbed the water, revealing them to be porous. Therefore, it was concluded that all 28 beads were natural hydrophane opal with natural color. Crazing was not observed in any of them.

Hydrophane opals are porous enough to absorb water, which can cause a change in appearance and a temporary increase in weight. It is therefore not advisable to immerse them in water (Fall 2013 Lab Notes, pp. 175–176).

This opal strand was remarkable due to the unusually bright and vibrant spectral play-of-color seen evenly across all 28 beads. Play-of-color in precious opal is caused by light interacting with stacked submicroscopic silica spheres. Light waves bend as they pass

*Figure 12. This spectacular opal strand displayed unusually bright, vibrant play-of-color across all 28 beads.*

between these spheres, causing the light to diffract into the spectral colors of the rainbow. The resulting color is determined by the size of the spheres. For example, approximately 0.1 micron spheres produce a violet color and approximately 0.2 micron spheres display a red color (https://www.gia.edu/opal-description).

*Michaela Stephan*

### Transparent RHODONITE with Clarity Enhancement

Recently the Carlsbad laboratory received a transparent vivid orangy red rhodonite for identification service (figure 13). Standard gemological testing revealed a double refractive index of 1.727–1.738, and a specific gravity of 3.66 was obtained. The stone was inert to both long-wave and short-wave UV light. These properties were consistent with rhodonite (R. Webster, *Gems*, 5th ed., rev. by P.G. Read, Butterworth-Heinemann, Oxford, 1994, p. 365). Rhodonite, with the formula $CaMn_3Mn[Si_5O_{15}]$ (mindat.org), is a member of the triclinic crystal system and occurs in manganese-bearing rocks.

During microscopic analysis, scattered curved needle-like inclusions (figure 14) were observed as well as fractures with clarity-enhancing residue that also contained high-relief areas where gas bubbles were trapped (figure 15). Although the source of this particular rhodonite is unknown, curved needle inclusions in transparent rhodonite from Brazil were previously reported in 2004 and 2008 (Fall 2004 GNI, pp. 260–261). The appearance of the needle-like inclusions was consistent with those previously identified as cummingtonite (P. Leverett et al., "Ca-Mg-Fe-rich rhodonite from the Morro da Mina mine, Conselheiro Lafaiete, Minas Gerais, Brazil," *The Mineralogical Record*, 2008, Vol. 39, pp. 125–130).

In addition to Brazil, Australia is a well-documented source of gem-quality rhodonite (P. Millsteed et al., "Inclusions in transparent gem rhodonite from Broken Hill, New South Wales, Australia," Fall 2005 *G&G*, pp. 246–254). Despite being clarity enhanced, this saturated gem-quality rhodonite was exceptional for its bright vivid color, transparency, and size.

*Amy Cooper*

*Figure 13. A large 11.32 ct rhodonite showing vivid orangy red color and visible needle-like inclusions.*

*Figure 14. These scattered randomly oriented curved needle-like inclusions are likely the mineral cummingtonite. Field of view 2.56 mm.*

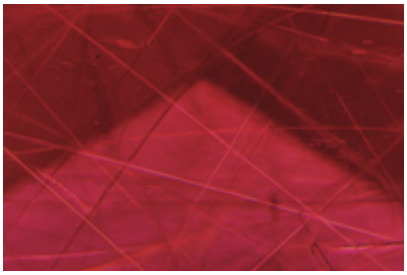

*Figure 15. Low-relief fractures with high-relief trapped gas bubbles offer proof of clarity enhancement in the faceted transparent rhodonite. Field of view 3.12 mm.*

## RUBY

### Amphibole Mineral Inclusions in Mozambique Ruby

Amphibole, a mineral supergroup with a diverse chemical composition of the general formula $AB_2C_5T_8O_{22}W_2$,

*Figure 16. Densely distributed amphibole inclusions in ruby. Field of view 9.40 mm.*

where A = □ (vacancy), $Na^{+}$, $K^{+}$, $Ca^{2+}$, $Pb^{2+}$, $Li^{+}$; B = $Na^{+}$, $Ca^{2+}$, $Mn^{2+}$, $Fe^{2+}$, $Mg^{2+}$, $Li^{+}$; C = $Mg^{2+}$, $Fe^{2+}$, $Mn^{2+}$, $Al^{3+}$, $Fe^{3+}$, $Mn^{3+}$, $Cr^{3+}$, $Ti^{4+}$, $Li^{+}$; T = $Si^{4+}$, $Al^{3+}$, $Ti^{4+}$, $Be^{2+}$; and W = $OH^{-}$, $O^{2-}$, $F^{-}$, $Cl^{-}$, is a collectors' item as a loose stone; its members are known as constituent minerals of nephrite (X. Feng et al., "Characterization of Mg and Fe contents in nephrite using Raman spectroscopy," Summer 2017 *G&G*, pp. 204–212). In addition, amphibole appears as crystal inclusions in both ruby and sapphire reported from Mozambique and Kashmir (e.g., Winter 2018 Lab Notes, pp. 435–436). Recently, the GIA lab in Tokyo received a Mozambique ruby densely included with rounded anhedral crystals (figures 16 and 17). The Raman pattern of the surface-reaching crystals most closely matched the RRUFF reference

*Figure 17. Photomicrograph of rounded anhedral amphibole crystals. Field of view 3.25 mm.*

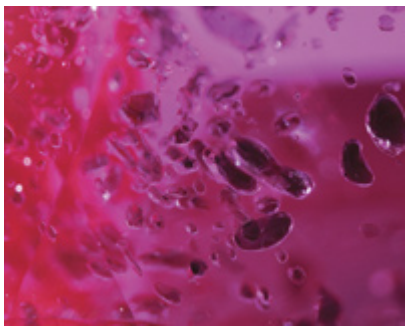

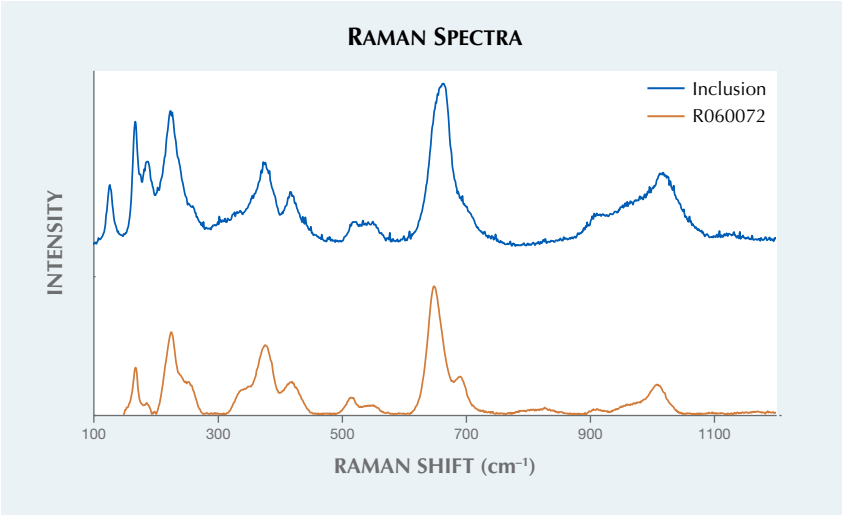


*Figure 18. The Raman spectrum of the amphibole mineral inclusions (blue) and the reference spectrum of pargasite from the RRUFF database (R060072).*

spectrum (no. 060072) of the calcic amphibole pargasite (figure 18). The Raman peak at 669 $cm^{-1}$ corresponded to the symmetric stretching vibration of T elements, which are tetrahedral ring structures composed mainly of the Si-$O_b$-Si linkage ($O_b$ = bridging oxygen) and often used to fingerprint various amphibole species (N. Waeselmann et al., "Nondestructive determination of the amphibole crystal-chemical formulae by Raman spectroscopy: One step closer," *Journal of Raman Spectroscopy*, Vol. 51, No. 9, 2020, pp. 1530–1548). The FTIR pattern showed some peaks between 3600 and 3800 $cm^{-1}$ in the principal OH-stretching region of octahedral metal components, which are C cations in the general formula of amphibole (figure 19). The FTIR pattern showed a peak at 3643 $cm^{-1}$ in addition to peaks at 3671 and 3704 $cm^{-1}$, suggesting the possibility that

*Figure 19. The FTIR spectrum of the Mozambique ruby, indicating the amphibole-related peaks between 3600 and 3800 $cm^{-1}$. The 3309 $cm^{-1}$ peak is associated with corundum.*

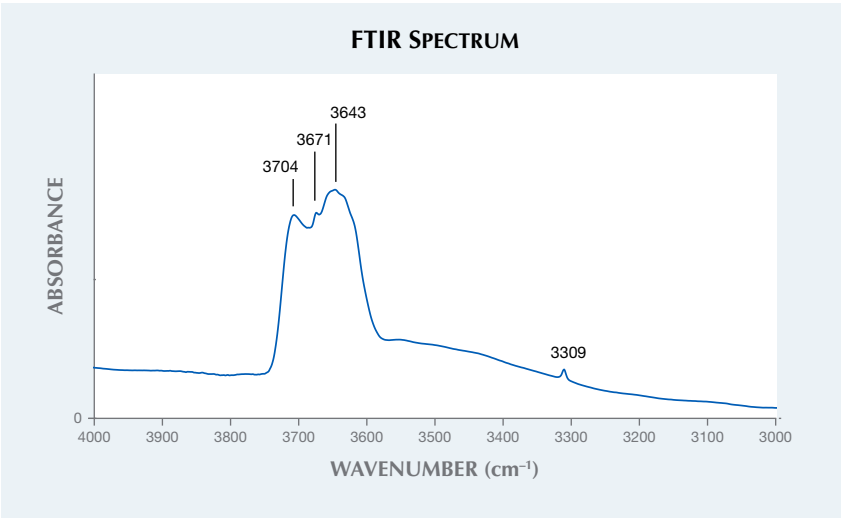

other elements such as Fe occupied those sites typical of pargasite in some portions (e.g., M.C. Day et al., "Gem amphiboles from Mogok, Myanmar: Crystal-structure refinement, infrared spectroscopy and short-range order–disorder in gem pargasite and fluoropargasite," *Mineralogical Magazine*, Vol. 83, No. 3, 2019, pp. 361–371). The FTIR spectra of corundum between 2000 and 5000 $cm^{-1}$ were very useful for the identification of mineral inclusions in corundum. This is the first known report of an FTIR pattern identifying amphibole mineral inclusions in corundum.

*Kazuko Saruwatari and Masumi Saito*

### Chrysoberyl Inclusions in Flux-Grown Ruby

The Tokyo laboratory recently received a 3.02 ct red pear-shaped mixed cut measuring 10.93 × 7.04 × 5.03 mm (figure 20). Standard gemological testing yielded a refractive index of 1.765–1.773; a hydrostatic specific gravity of 4.00; absorption lines at 693, 476, and 468 nm; and a broad absorption band between 500 nm and 610 nm seen using a handheld spectroscope. All of these properties were consistent with ruby. The stone displayed strong red fluorescence under both long-wave and short-wave UV.

*Figure 20. This ruby proved to be a flux-grown synthetic ruby with chrysoberyl inclusions.*

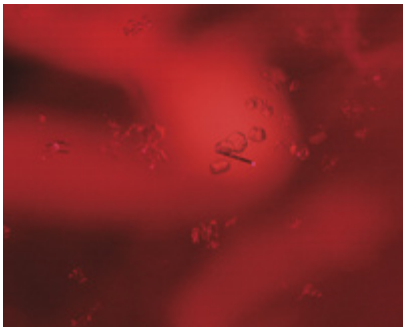

*Figure 21. These natural-looking hexagonal colorless crystals and the small nest of inclusions in the flux-grown ruby (top of image and around the hexagonal crystals) could be mistaken for natural corundum inclusions. Field of view 1.41 mm.*

Microscopic examination revealed numerous hexagonal colorless inclusions as well as small colorless inclusions that resembled zircon nests often found in natural corundum (figure 21). Also observed were features suggesting the possibility of flux-grown corundum: hexagonal dark reflective long prisms and platelets (figure 22) and healed fissures filled with flux residues (figure 23).

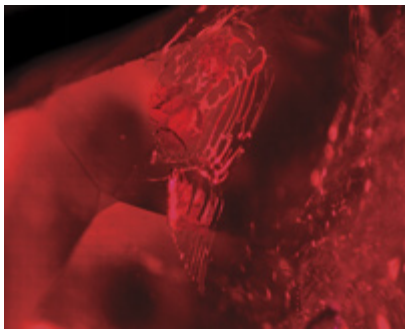

*Figure 23. Fingerprints in the flux-grown ruby could also be mistaken for natural residue-filled fingerprints. Field of view 1.23 mm.*

Laser ablation–inductively coupled plasma–mass spectrometry (LA-ICP-MS) detected high amounts of Be (35.3–37.1 ppma), Cr (1733.5–2047.2 ppma), Rh (0.6–1.0 ppma), and Pt (0.5–1.1 ppma). Elements normally present in natural corundum such as Mg, Ga, and V were not detected. The chemistry indicated a flux growth process.

Earlier work has shown numerous transparent, colorless hexagonal tabular "ghost-like" inclusions in Chatham flux-grown sapphire (R.E. Kane, "The gemological properties of Chatham flux-grown synthetic orange sapphire and synthetic blue sapphire," Fall 1982 *G&G*, pp. 140–153). In that study, X-ray diffraction analysis (XRD) revealed that the pattern of the ghost-like inclusions was identi-

*Figure 22. The hexagonal dark reflective long prisms (left) and platelets (right) observed in the sample are common inclusions in flux-grown synthetic corundum. Field of view 1.28 mm.*

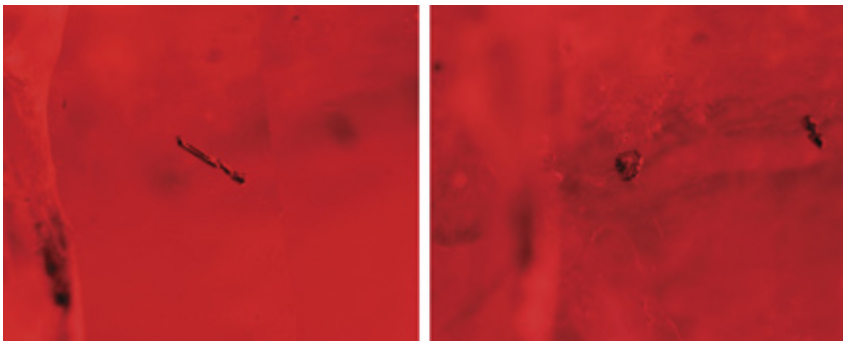

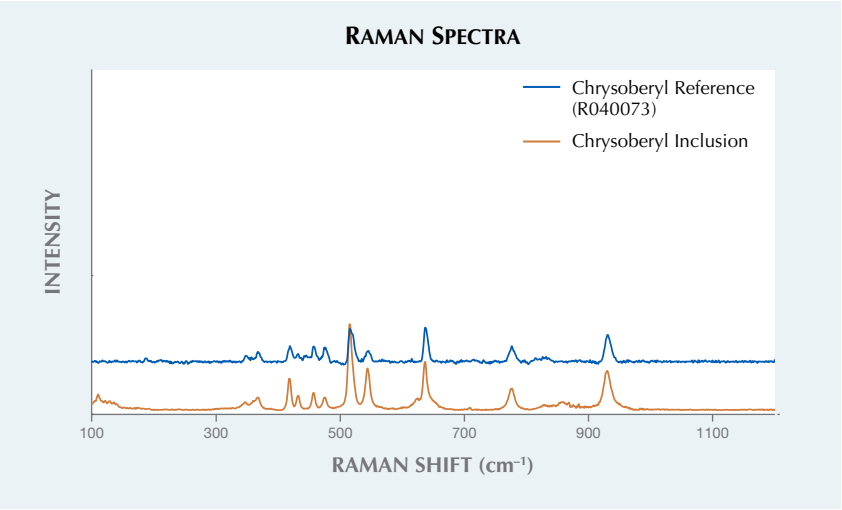


*Figure 24. The Raman spectrum of the chrysoberyl inclusion compared to that of the known reference.*

cal to that of chrysoberyl. That study also stated that Chatham, who was successful in synthesizing sapphire by the flux method, added heavy concentrations of beryllium, which explained the presence of chrysoberyl and the high beryllium trace element content. More recently, natural-looking transparent hexagonal crystals in a flux-grown pink sapphire have also been reported (Fall 2017 Lab Notes, pp. 367–368). There was no surface-reaching transparent crystal in that pink synthetic sapphire, but the small amounts of beryllium suggested the possibility of chrysoberyl. In the present laboratory-grown ruby, fortunately, one of the transparent crystals reached the surface. With Raman spectroscopy, we were able to identify it as chrysoberyl (figure 24).

The beryllium concentration of this laboratory-grown ruby (up to 37 ppma) indicated possible beryllium diffusion treatment. High chromium (up to 2047 ppma) resulted in a vivid red color. With such a highly saturated bodycolor, we cannot deny the possibility of beryllium diffusion, though the signature orange rim was not found using immersion techniques. The numerous chrysoberyl crystals offer important evidence that the beryllium was already excised during the flux growth process. Beryllium diffusion of corundum requires exposure to extreme heat (above 1780°C; J.L. Emmett et. al., "Beryllium diffusion of ruby and sapphire," Summer 2003 *G&G*, pp. 84–135). These chrysoberyl inclusions do not show the typical indications following heat treatment, meaning this stone was not beryllium diffused after its growth.

With LA-ICP-MS and Raman spectroscopy, we were able to confirm that flux-grown laboratory-grown ruby with high beryllium content could indicate the presence of natural-looking chrysoberyl crystals.

*Yuxiao Li*

*PHOTO CREDITS*
*Sean-Andrew Z. Pyle—1; Tyler Smith—2, 3; Ellen Barrie—4, 5, 6; Nuttapol Kitdee—7; Kwanreun Lawanwong—8; Michaela Stephan—10, 11; Angelica Sanchez—12; Diego Sanchez—13; Nathan Renfro—14, 15; Kazuko Saruwatari—16; Masumi Saito—17; Shunsuke Nagai—20; Yuxiao Li—21, 22, 23*